Nanoscale

Accepted Manuscript

This article can be cited before page numbers have been issued, to do this please use: G. Tian, Z. Li, J. Gao, W. Han, X. Ma, L. Sun and H. Wang, *Nanoscale*, 2025, DOI: 10.1039/D5NR02365C.

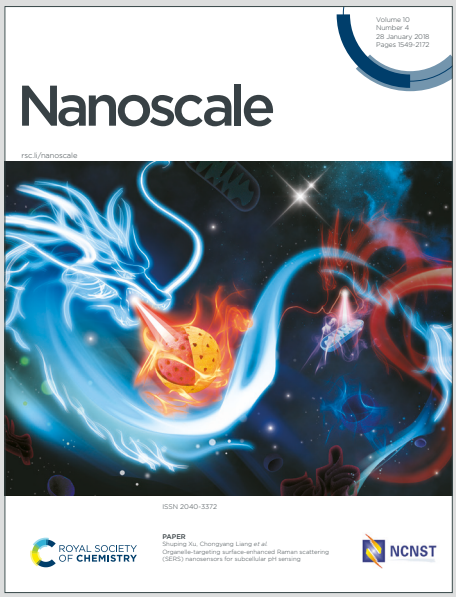

ROYAL SOCIETY OF CHEMISTRY

rsc.li/nanoscale

View Article Online
DOI: 10.1039/D5NR02365C

Synergistic effect of Mg and Ti ions by dual-site modulation strategy induces enhanced ordering and electrochemical performance of layered cathode for sodium-ion batteries

Gengfang Tian[1], Jianxiang Gao[1], Zheng-Yao Li[1*], Limei Sun[1], Wenze Han[2*], Hongliang Wang[1], Xiaobai Ma[1*]

[1] Neutron Scattering Laboratory, Department of Nuclear Physics, China Institute of Atomic Energy, Beijing 102413, People's Republic of China

[2] Research Institute of Physical and Chemical Engineering of Nuclear Industry, Tianjin, 300180, People's Republic of China

*E-mail: lizhengyao@ciae.ac.cn (Z. -Y. Li)

*E-mail: hanwenze2003@163.com (W. Han)

*E-mail: maxiaobai@ciae.ac.cn (X. Ma)

ABSTRACT

Herein, high-performance P2-$Na_{2/3}Mg_{1/18}[Ni_{1/4}Ti_{5/36}Mn_{11/18}]O_2$ (NMNTM) cathode material is designed via a dual-site modulation strategy of Mg/Ti ions in different crystallographic sites. Unlike the $P6_3/mmc$ space group identified by X-ray diffraction, neutron diffraction confirms the distributions of Mg-ion in Na sites and Ti in transition-metal sites, and a larger super cell structure with the $P6_3$ space group, indicating the existence of superlattice ordering in NMNTM. Electrochemically inert Mg/Ti ions do not smooth the charge/discharge profiles, but lead to the staircase-like voltage profiles upon electrochemical cycling, which is due to enhanced superlattice ordering confirmed by neutron diffraction. However, Mg/Ti ions effectively inhibits the P2-O2 phase transition at high voltage ranges, indicating the phase-transition-free solid-solution reaction. NMNTM delivers a reversible capacity of 113 mAh g^{-1} with largely improved rate capability, corresponding to 87% of theoretical capacity, and a great capacity retention of 80.2% after 150 cycles. Dual-site modulation of Mg and Ti ions

in different crystallographic sites is beneficial for achieving the synergistic effect, which effectively tunes the Mn^{3+}/Mn^{4+} ratio to avoid the Jahn-Teller distortion by eliminating Mn^{3+} ions and resulting structure degradation benefiting from Mg ions, leads to pillar effect of Mg ions in Na sites, enhances structure integrity by strong Ti-O bond in contrast to Mn-O bond, suppresses the P2-O2 transition and promotes the Na-ion movement, thereby improving the electrochemical performance of NMNTM.

Keywords: $Na_{2/3}Mg_{1/18}[Ni_{1/4}Ti_{5/36}Mn_{11/18}]O_2$; neutron diffraction; Mg doping; Ti doping; sodium ion battery

View Article Online
DOI: 10.1039/D5NR02365C

1 Introduction

As an appealing candidate for low-cost energy storage system or a great complementary to lithium-ion batteries (LIBs), sodium-ion batteries (SIBs) are very promising for large-scale energy storage applications at room temperature, owing to the easy availability of Na resources, enhanced safety and great electrochemical performance. To enhance the entire practical property of SIBs, exploring high-performance cathode materials is one of key factors to promote the advance in SIBs. Currently, a series of cathode materials have been designed and investigated such as the polyanion compounds, Prussian Blue and Na-based transition-metal (TM) oxides (Layered and Tunnel types), and each one has its advantages and disadvantages. In contrast, Na-based layered transition-metal oxides (Na_xTMO_2, where TM represents a transition metal or their mixture, such as Mn, Ni and Fe…) features alternating arranges of TMO_2 layers (Edge-sharing TMO_6 octahedra form the TMO_2 layers in ab plane) and Na-ion layers along the c-direction, which are very attractive group due to their diverse crystal structure types (such as P2, P3, O3 and P'2 types), dense structure and high theoretical capacity[1-3].

In these structures, P2-type layered oxides involve relatively large space of prismatic sites to accommodate Na-ion during the removal and uptake of Na ions, providing easier Na^+ diffusion and improved rate-capability compared with their O3-type counterparts. However, P2-Na_xTMO_2 cathodes usually experience a series of phase transitions at high voltage ranges, in particular the detrimental P2-O2 transition to cause a huge volume change (> 20%) and sluggish Na-ion mobility in the O2 structure, thereby degrading the structure integrity and the cycling capacity upon charging and discharging. For instance, the significant reduction in cycling stability is caused by P2-O2 phase transition upon being charged over 4.0 V in Na-Ni-Mn-O composition systems [4-6]. On the other hand, Mn-based P2-Na_xTMO_2 materials, as one of the important P2-type layered cathode materials, are very fascinating due to the cost-effective, non-toxic, great abundance and good electrochemistry of Mn element, but Jahn-Teller effect usually occurs in Mn-based cathode materials due to the Mn^{3+} in

pristine materials or being induced by Mn^{3+}/Mn^{4+} electrochemical reaction during the charge/discharge process. Jahn-Teller effect gives rise to severe lattice degradation, reduced Na-ion diffusivity in Mn-based cathode materials[5, 7-9], thereby resulting in poor crystal stability and rapid property failure. For example, P2-$Na_{0.67}MnO_2$ can deliver a high specific capacity of over 160 mAh g^{-1}, but the cycling capacity decay is largely decreased during repeated electrochemical cycling, due to the Jahn-Teller effect and complex phase transitions[10, 11].

To suppress the P2-O2 phase transition and alleviate the Jahn-Teller distortion caused by Mn^{3+} ions, bulk substitution has been proven to be a rational strategy to stabilize the structure and enhance electrochemical performance, such as Mg, Zn, Li, K, Al, and Ti ions[12-20]. An early study has found that Mg-ion can hinder phase transition and smooth charge/discharge profiles to realize a facile electrochemistry[12], and subsequently a series of Mg-doped P2-Na_xTMO_2 cathode materials with Mg-ion in different crystallographic sites have been exploited and studied[21-25]. Li-doping significantly delays the phase transformation up to 4.4 V in P2-$Na_{0.80}[Li_{0.12}Ni_{0.22}Mn_{0.66}]O_2$ and displays smooth charge/discharge profiles, offering great rate capability[26]. In contrast, P2-$Na_{0.67}Mn_{0.6}Ni_{0.2}Li_{0.2}O_2$ shows little change in the lattice parameters and stable P2 crystal structure after Li-doping, leading to sloping voltage profiles and excellent cycle life[19]. Different from reported Li-doped cathode materials, a recent study has found that P2-$Na_{0.67}Li_{0.1}Ni_{0.3}Mn_{0.6}O_2$ undergoes a P2-OP4 phase transformation when being charged to 4.5 V, and surprisingly the $Ni^{2.8+}/Ni^{4+}$ redox pairs participate in electrochemical reaction, instead of the well-known Ni^{2+}/Ni^{4+} couples[18]. It is also shown that Zn content can affect phase transition, such as the suppressed the P2-O2 phase transition in $Na_{0.67}Ni_{0.26}Zn_{0.07}Mn_{0.67}O_2$, but a P2-Z phase transition occurs in $Na_{0.6}Mn_{0.7}Ni_{0.15}Zn_{0.15}O_2$ [13, 27]. In addition, Ti^{4+} has a larger ionic radius (0.605 Å) than that of Mn^{4+} (0.53 Å) and stronger bonding energy of Ti-O (666.5 kJ mol^{-1}) than Mn-O bond (402 kJ mol^{-1}), therefore, the substitution of Mn with Ti can improve the average working voltage, enhance the structure stability and cycling performance[20, 28]. Apart from the P2-O2 phase transition at high voltage ranges, the existing superstructure ordering is also believed to deteriorate the electrochemical

performance of P2-type layered cathodes, and eliminating superstructure ordering is a rational approach to improve their electrochemical performance[29, 30]. However, several studies have announced that P2-Na_xTMO_2 materials with superstructure ordering in structure can also display comparable electrochemical performance to the ordering-free cathode materials (disordered cathode materials), through suitable element-ion to tune the material structure[16, 23, 24, 31-33].

Herein, a dual-site modulation strategy in both Na and Mn sites is proposed to strengthen the crystal structure and enhance the electrochemical performance of P2-$Na_{2/3}[Ni_{1/4}Mn_{3/4}]O_2$ (NNM) cathode material. P2-$Na_{2/3}[Ni_{1/4}Mn_{3/4}]O_2$ (NNM) is a medium Ni-content Na-Ni-Mn-O composition compared with well-studied P2-$Na_{2/3}Ni_{1/3}Mn_{2/3}O_2$, which is cost-effective with a relatively low Na-content[6]. Mg ions are incorporated into the Na sites, which serves as stable pillars to avoid the structure collapse, creating a robust crystal structure upon removal of Na-ion out of the P2-structrue host. Partial substitution of Ti^{4+} for Mn^{4+} in the TM layers can slightly stabilize the crystal structure and also improve the working voltage. As a consequence, P2-$Na_{2/3}Mg_{1/18}[Ni_{1/4}Ti_{5/36}Mn_{11/18}]O_2$ (NMNTM) was designed and investigated by a series of physical/electrochemical tests. It should be noted that Mg and Ti ions effectively eliminate the Mn^{3+} to avoid the Jahn-Teller distortion, in particular the Mg-ion, considering the Mn^{3+} ions in P2-$Na_{2/3}[Ni_{1/4}\ Mn^{3+}{}_{1/6}Mn^{4+}{}_{7/12}]O_2$ (NNM). Though Mg and Ti ion are inert, NMNTM still shows staircase-like voltage curves during the charge/discharge process, which is caused by enhanced ordering by dual-site modulation of Mg/Ti. Unlike the typical P2-O2 phase transition in NNM cathode, NMNTM maintains the P2 structure within the whole voltage range confirmed by ex situ X-ray diffraction tests. NMNTM displays largely improved rate capability and cycle-life within the voltage range of 2.5-4.3 V, and the enhancement in electrochemical performance is ascribed to the synergistic effect of dual-site modulation of Mg/Ti ions, which promotes Na-ion movement by GITT tests, inhibits the P2-O2 phase transition, hinders the Jahn-Teller effect caused by eliminating Mn^{3+}, serves as pillars of Mg ions in Na sites to avoid structure collapse and Ti-ion in the TM layer to stabilize crystal structure.

View Article Online
DOI: 10.1039/D5NR02365C

2 Experimental Section

2.1 Synthesis of Cathode Materials

$Na_{2/3}Mg_{1/18}[Ni_{1/4}Ti_{5/36}Mn_{11/18}]O_2$ (NMNTM) was prepared by a simple sol-gel approach. Stoichiometric ratio of $NaNO_3$ (5% excess), $Ni(NO_3)_2$, $Mg(CH_3COO)_2$, TiO_2 and $Mn(CH_3COO)_2$ were dissolved into a citric acid (CA) solution to form a wet sol under magnetic stirring at room temperature (Mole ratio of CA : metal ions = 2 : 1). The wet sol was maintained at 80 °C for 5 hours and then dried at 120 °C overnight to obtain a dry gel. Consequently, the dry gel was sintered at 500°C for 5 hours then at 900 °C for 10 hours in air, respectively. P2-$Na_{2/3}[Ni_{1/4}Mn_{3/4}]O_2$ (NNM) material was synthesized by the same method and process with raw materials of $NaNO_3$ (5% excess), $Ni(NO_3)_2$ and $Mn(CH_3COO)_2$. All the samples were stored in Ar-filled glovebox.

2.2 Material Characterization and Analysis

Powder X-ray diffraction (XRD) patterns were collected by a Bruker diffractometer (advance D8) using Cu Ka radiation in the scan range of 10-80°. High-Resolution Powder Diffractometer (HRPD) was used to characterize the crystal structures of NNM and NMNTM materiasl, which is located at the China Advanced Research Reactor (CARR) at China Institute of Atomic Energy. The neutron wavelength is 1.888 Å and the scanning step is 0.07°. The lattice parameters were refined by Fullprof software based on Rietveld method. High-resolution transmission electron microscope (HRTEM) experiments were carried out on a Tecnai G2 F20 S-TWIN (200 kV), and Scanning electron microscopy (SEM) tests were performed on a Hitachi S-4800 apparatus (2 kV). X-ray photoelectron spectroscopy (Thermo Scientific ESCALAB 250Xi) using Al K_a X-ray radiation was used to analyze the oxidation state change for ex situ experiments. Coin cells were firstly charged to 4.3 V at 0.1 C and then discharged to 2.5 V For the ex situ XRD tests, and then the cells were disassembled in Ar-filled glovebox. At last, the cathodes were sealed by Capton films to carry out the ex situ XRD measurements.

2.3 Electrochemical Characterization

Electrochemical performance tests were completed using CR2025 coin cells. The active materials (75 wt%), Super P carbon (15 wt%), and poly(vinylidene fluoride) (PVDF, 10 wt%) were mixed using N-methylpyrrolidinone (NMP) to generate the slurries at first, then they were uniformly coated onto pure Al foil current collectors followed by being dried under vacuum at 120°C for 12 h at least. $NaClO_4$ (1mol L^{-1}) in a mixture of propylene carbonate (PC) with adding 5% FEC as additive was used as electrolyte. Glass fiber membranes GF/D (Whatman) were used as separators. Galvanostatic charge-discharge and Galvanostatic intermittent titration technique (GITT) tests were performed on a NEWARE battery test station (Wuhan, China) in the voltage range of 2.5 - 4.3 V Vs. Na^+/Na at room temperature. Cyclic voltammetry (CV) data were collected at 0.1 mV s^{-1} between 2.5 and 4.3 V on an electrochemical workstation (CHI660E, Shanghai Chenhua, China).

3 Result and discussions

3.1 Material Structure Characterization by XRD and NPD

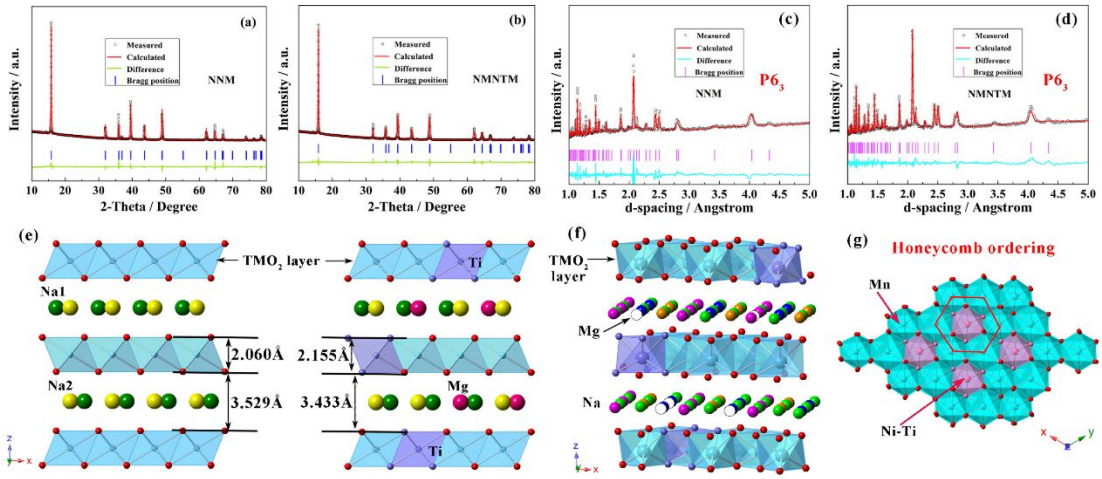

Fig. 1 Refined X-ray diffraction (XRD) results of (a) NNM, (b) NMNTM, and refined neutron diffraction data of (c) NNM and (d) NMNTM using $P6_3$ model. (e) Comparison of crystal structure change of NNM and NMNTM, (f) structure model using $P6_3$ space group (Rose-red sphere: Na1, Green sphere: Na2, Blue sphere: Na3 and Orange sphere: Na4, Purple sphere: Ti), and (g) the honeycomb ordering structure in the TM layers in NMNTM material using $P6_3$ model based on neutron diffraction data.

Fig. 1a-b exhibit the X-ray diffraction (XRD) data and refinements based on Rietveld

View Article Online
DOI: 10.1039/D5NR02365C

method of as-prepared P2-$Na_{2/3}$ $[Ni_{1/4}Mn_{3/4}]O_2$ (NNM) and P2-$Na_{2/3}Mg_{1/18}[Ni_{1/4}Ti_{5/36}Mn_{11/18}]O_2$ (NMNTM). All the diffraction peaks of both samples can be assigned to P2-type layered structure with the $P6_3/mmc$ space group, and the absence of other diffraction peak indicates a single-phase composition after Mg and Ti ions co-doping[26, 31, 33, 34]. Table S1-S2 present the detailed crystallographic information of NNM and NMNTM materials. The lattice parameters were calculated by FullProf software, which are a = 2.8801 Å and c = 11.1795 Å for the NNM material, and a = 2.8949 Å and c = 11.1774 Å for the NMNTM material, respectively. The substitution of Ti for Mn in the TM layer induce a little increase in lattice parameter *a*, which is due to the relatively large ionic radius of Ti^{4+} (0.605 Å) compared with Mn^{4+} (0.53 Å). In P2-Na_xTMO_2 framework, TMO_2 layers composed of TMO_6 octahedrons and Na-ion layers are alternatively arranged along the c-axis to form the layered structure, and Na ions in the Na-ion layer can serve as screening effect between adjacent TMO_2 layers to keep the charge balance and structure stability. It has been proven that high Na-content in P2-Na_xTMO_2 usually leads to a reduced lattice parameter *c* due to the enhanced screening effect[35, 36]. Therefore, lattice parameter *c* shows a slight reduction in NMNTM, which is associated with Mg-doping to improve the number of positive charge in the Na-ion layer, resulting in decreased Coulombic repulsion between adjacent O^{2-}- O^{2-} ions[37]. Moreover, the thickness of TMO_2 layers increases from 2.060 Å in NNM to 2.155 Å in NMNTM, which is in good accordance with the difference in ionic radius of Ti^{4+} (0.605 Å) compared with Mn^{4+} (0.53 Å), as shown in Fig. 1e. The space for Na-ion diffusion is slightly constricted 3.529 Å in NNM to 3.433 Å in NMNTM after doping, and this change is mainly due to doped Mg-ion in the Na sites, rather than in the TM sites. Such a reduction in Na-ion layers spacing size has also been observed in several layered oxide materials[38, 39].

To identify the locations of Mg/Ti and the possible superlattice ordering in structure, neutron diffractidon tests were therefore carried out to disclose the possible superlattice ordering and the different distributions of doped Mg and Ti ions, due to the similar scattering ability of Ni and Mn to X-ray. Fig. S1 compares the neutron powder diffraction (NPD) data of NNM and NMNTM sample using $P6_3/mmc$ and $P6_3$ space

groups, indicating a distinct difference in structure. Different from the unit cell structural model with the $P6_3/mmc$ space group characterized by XRD, it is evident that $P6_3/mmc$ model is unsuitable for explaining the NPD data, due to the existence of superstructure ordering in both materials[24, 26, 31, 33, 40]. Besides, Fig. S1 also illustrates the enhanced intensity of superstructure peaks labeled by green arrows, which implies the enhanced ordering benefiting from dual-site modulation of Mg/Ti in different crystallographic sites. This enhancement in superlattice ordering is similar to Mg-doping in both the Na-ion and TM layers[23], but different from the decreased ordering in layered oxide cathode by Li/Ti co-doping in the TM layers[33]. On the other hand, regarding the difference in coherent neutron scattering lengths (Ti = -3.37 fm and Mg = 5.37 fm), neutron diffraction also indicates that Mg ions enter the Na-ion layers and Ti ions occupy the TM sites. Note that Mg^{2+} in Na sites can serve as a pillars to restrict the structural change during the charge/discharge process, thereby significantly improving the cycling stability[41, 42]. Fig. 1c-d exhibits the refinement of NNM and NMNTM sample based on NPD data using a larger $\sqrt{3}a \times \sqrt{3}a \times c$ type super cell with the $P6_3$ space group, and the detailed crystallographic sites and occupy are presented in Table S3-S4. The result is consistent previous studies[23, 24, 31, 33, 43]. There are three kinds of ordering structures in P2-type layered materials so far, including the Na^+/vacancy ordering in the Na-ion layer, TM ordering and charge ordering in the TM layer, which impacts each other[29, 30]. Fig. 1f clearly illustrates the crystal structure model with the $P6_3$ space group, in which involves four Na sites, three TM sites and two O sites. Fig. 1g further exhibits the existing TM ordering in the TM layer, forming a honeycomb ordering arrange between Ni/Ti and Mn ions in NMNTM[16, 22, 33, 44, 45]. The calculated lattice parameters of a = 5.0102 Å and c = 11.1649 Å for the NMNT sample, and a = 4.9989 Å and c = 11.1634 Å for the NNM sample. Lattice parameter *a* by NPD data refinement using super cell model is 1.732 times higher than *a* value by XRD data using unit cell model ($P6_3/mmc$), which is consistent with the $\sqrt{3}a \times \sqrt{3}a \times c$ super cell ($P6_3$ space group) relative to the unit cell ($P6_3/mmc$ space group). Therefore, in contrast to XRD, neutron diffraction is in favor of studying the possible

superlattice ordering in P2-type layred oxide cathodes, offering more crystal structure information to study the structure-property relationship of layered materials.

3.2 Morphology and Structure Analysis

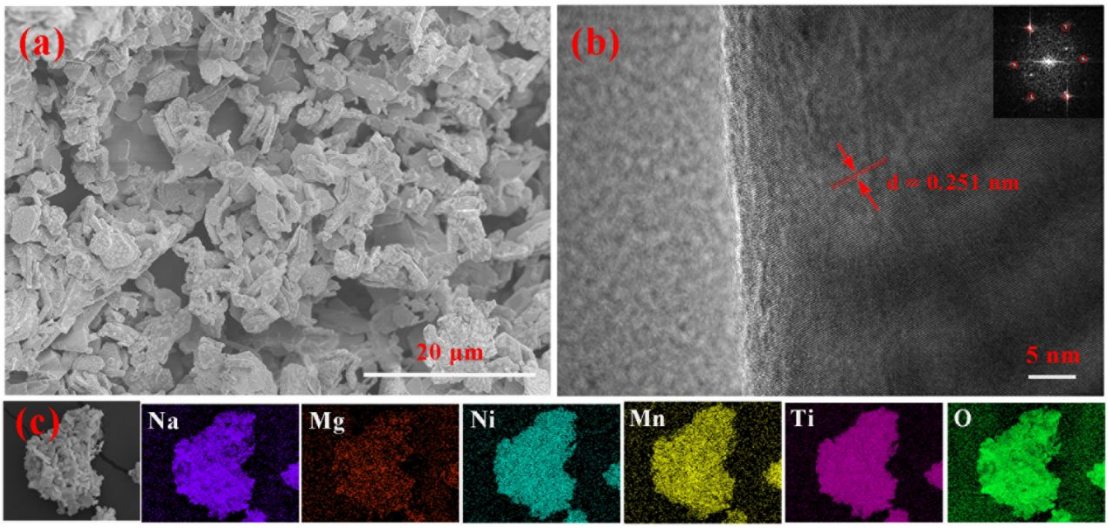

Fig. 2 (a) SEM, (b) HRTEM images and (c) element distribution mapping by EDS spectra of NMNTM sample.

Fig. 2a shows the scanning electron microscopy (SEM) image of as-prepared NMNTM sample. NMNTM exhibits uniformly plate-like morphology with a thickness of several micrometers. Fig. S2 shows the SEM image of NNM material, which has the similar morphology and size with NMNTM material. Na, Mg, Ni, Ti, Mn and O element are uniformly distributed in NMNTM material according to the corresponding energy-dispersive spectroscopy (EDS) analysis coupled with SEM tests, as shown in Fig. 2c. High-resolution transmission electron microscope (HRTEM) with fast fourier transform (FFT) images in Fig. 2b reveals a high crystallinity and a distance of about 0.251 nm between neighboring lattice fringes, corresponding to the (100) plane of the $P6_3/mmc$ model in NMNTM sample.

3.3 Electrochemical Performance Analysis

View Article Online
DOI: 10.1039/D5NR02365C

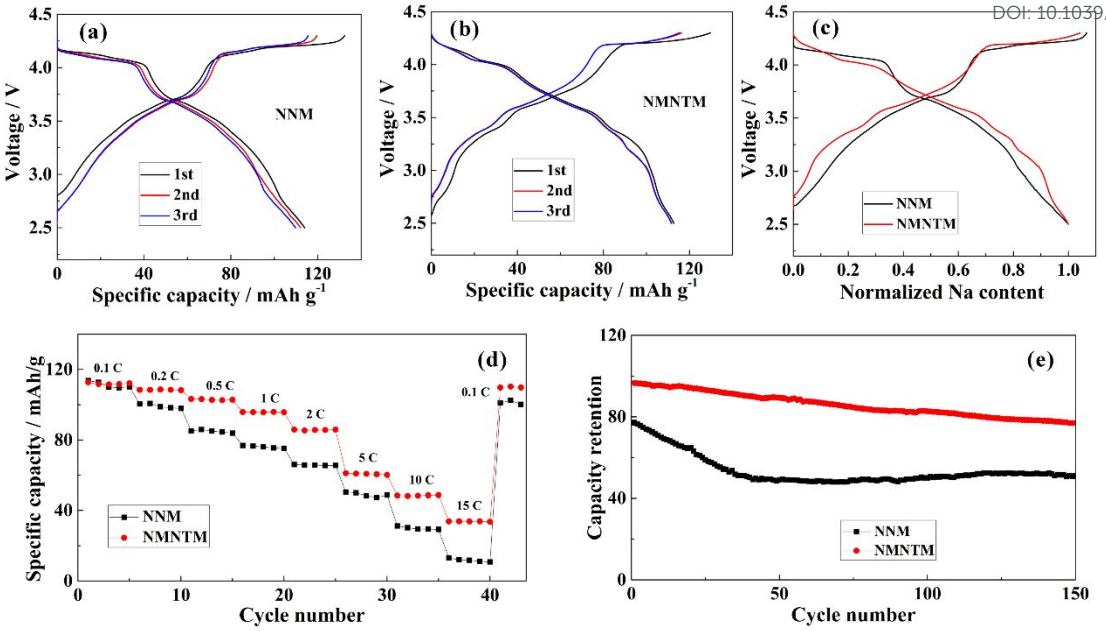

Fig. 3 Initial three charge/discharge profiles of (a) NNM and (b) NMNTM. (c) Normalized charge and discharge profiles of NNM and NMNTM cathodes during the second cycle at 0.1 C. Comparison of (d) rate capabilities at different rates and (e) cycling performance of NNM and NMNTM cathodes at a rate of 1 C.

Fig. 3a-b display the initial three charge and discharge curves of NNM and NMNTM cathodes at 0.1 C in the voltage range of 2.5 - 4.3 V at room temperature. NNM cathode exhibits distinct voltage plateaus over 4.0 V and smooth charge/discharge profiles below 4.0 V. And the voltage plateaus result from the P2-O2 phase transition at high voltage ranges in Na-Ni-Mn-O composition systems[6, 40, 46]. NMNTM also shows long voltage plateaus in the charge/discharge profiles above 4.0 V, but several small voltage plateaus below 4.0 V. Apart from the Ni^{2+}/Ni^{4+} redox reaction, this change is also closely related to the enhanced ordering in NMNTM by dual-site modulation of Mg/Ti ions in different sites upon electrochemical cycling, according to neutron diffraction and ex situ XRD tests in the following discussion. It should be noted that single Ti-doping in the TM layer or Mg-doping in Na sites disrupts the superlattice ordering and smooth voltage curves in P2-type layered oxide cathode materials[30, 34], Mg/Ti ions co-doping in different sites enhances the ordering to induce the staircase-like voltage curves in the study. Contrary to several reports that inert Mg

or Ti ions can smooth the charge/discharge curves[12, 21, 30], NMNTM still exhibits step-like voltage profiles due to the doping of Mg/Ti ions. Moreover, Fig. 3c shows the normalized charge/discharge profiles at the second cycle, it is shown that NMNTM exhibits a little higher average working voltage than NNM cathode, which is associated with Ti-doping in the TM layer [20].

NNM and NMNTM cathode deliver close initial specific discharge capacities of 114 mAh g^{-1} and 113 mAh g^{-1} at 0.1 C (1 C = 130 mAh g^{-1} based on Ni^{2+}/Ni^{4+} reaction) in Fig. 3a-b, respectively. Therefore, inactive Mg and Ti co-doping does not affect the practical discharge capacity due to the constant Ni-content in both materials. However, the rate capability decay of NNM cathode is severe with increasing the current density in contrast to NMNTM cathode, as shown in Fig. 3d. The reversible capacities of NMNTM are about 109, 102, 96, 86, 61, 49 and 34 mAh g^{-1} at the rates of 0.2 C, 0.5 C, 1 C, 2 C, 5 C, 10 C and 15 C, respectively, which largely exceed those of 99, 85, 76, 65, 49, 30 and 12 mAh g^{-1} at the same rates for the NNM cathode. And the specific capacities of NMNTM and NNM cathodes are back to about 109 and 101 mAh g^{-1} at 0.1 C after the high rate of 15 C, respectively. The results confirm the significant enhancement in rate performance after dual-site modulation strategy of Mg and Ti in different crystallographic sites. Fig. 3e compares the cycle performance of NNM and NMNTM cathodes at a rate of 1 C between 2.5 and 4.3 V. The reversible specific capacity of NMNTM cathode is about 77 mAh g^{-1} at 150th cycle, which corresponds to a capacity retention of 80.2%. In contrast, the discharge capacity of NNM cathode decreases to about 50 mAh g^{-1} at the 150th cycle compared with 76 mAh g^{-1} at the 1st cycle, corresponding to 65.8% capacity retention. The P2-O2 phase transition at high voltage ranges can account for the poor cycling stability of NNM cathode. Extraction of more Na ions out of the Na-ion layer in the P2 phase framework can bring out the structural collapse or irreversible phase transition, like the typical P2-O2 transition, but doped Mg ions in Na sites can serve as stable pillars to prevent the structural collapse and stabilize the lattice crystal upon extracting more Na ions. Therefore, the enhanced electrochemical performance of NMNTM can be ascribed to the pillar effect of Mg-ion in Na sites, the inhibited P2-O2 phase transition to create a phase-transition-free

cathode, suppressed Jahn-Teller effect by eliminating Mn^{3+} in NMNTM material to avoid the structural distortion and also the strong bonding energy of Ti-O relative to Mn-O to strengthen the lattice structure in NMNTM cathode upon extracting/inserting Na-ion[16, 25, 28, 32, 41, 42]. Different from the improved electrochemical performance due to the reduced superlattice ordering by Li/Ti co-doping in the TM layer[33], dual-site modulation of Mg and Ti ions enhances the ordering in NMNTM, but NMNTM still shows great electrochemical performance. Therefore, ordered layered cathode materials still can exhibit promising electrochemical performance through adequate alien-ion doping to tailor the crystal structure.

3.4 Electrochemistry Mechanism Analysis

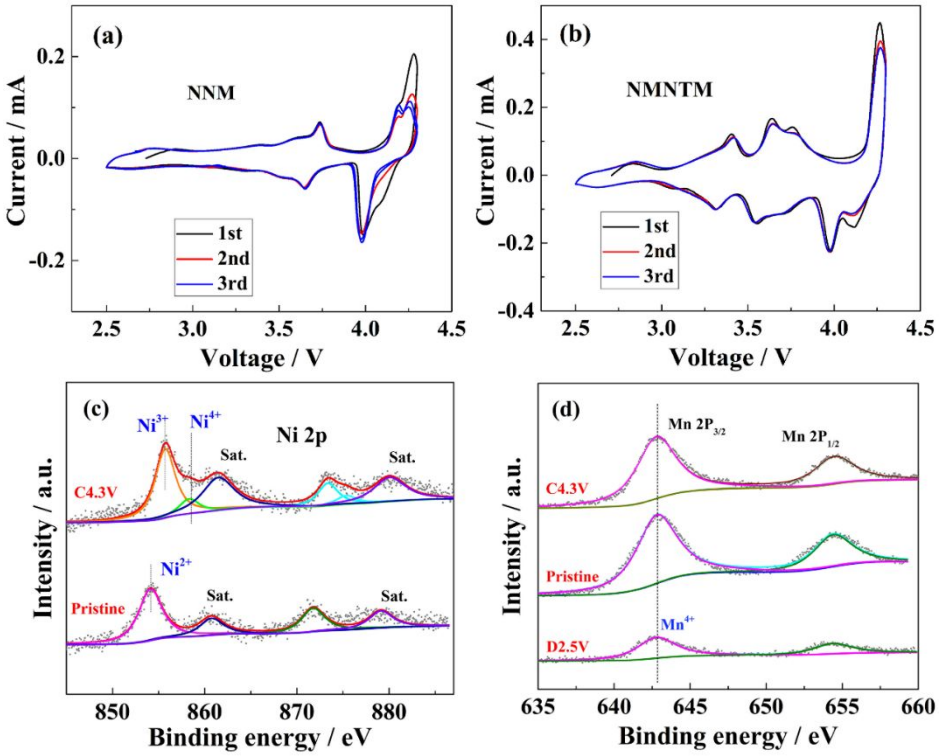

Fig. 4 CV plots of (a) NNM and (b) NMNTM cathodes at 0.1 mV s^{-1}. Ex situ XPS data and fitting results of (c) Ni-ion and (d) Mn-ion at different charged states for the NMNTM cathode.

To reveal the electrochemical reaction mechanism, cyclic voltammetry (CV) and ex situ X-ray photoelectron spectroscopy (XPS) tests were employed. Fig. 4a-b compare

the CV plots of NNM and NMNTM cathodes at 0.1 mV s^{-1}. A pair of strong oxidation/reduction peaks at ≳ 4.0 V in Fig. 4a indicate the typical P2-O2 phase transition that occurs in NNM cathode[6, 40]. The oxidation/reduction peaks in CV plots below 4.0 V can be ascribed to the Ni^{2+}/Ni^{4+} redox couples reaction upon charging and discharging. On the contrary, NMNTM exhibits a couple of strong oxidation/reduction peaks with good overlapping at ≳ 4.0 V and three pairs of oxidation/reduction peaks below 4.0 V, which are related to the Ni^{2+}/Ni^{4+} couples and superlattice ordering in NMNTM[23, 40, 47], rather than the P2-O2 transition, on the basis of neutron diffraction and ex situ XRD tests in the following discussion. In contrast to Mn^{3+}/Mn^{4+} ions in NNM material[6, 40], Fig. 4d shows that Mn ions in NMNTM material are in +4 oxidation state without any Mn^{3+} ions, indicating that Mn^{3+} are effectively eliminated by Mg^{2+} and Ti^{4+} co-doping, in particular the Mg^{2+} ions, due to the same valence state of Ti^{4+} and Mn^{4+} in TM layers. Therefore, Jahn-Teller distortion associated with high spin Mn^{3+} ions is largely suppressed in NMNTM, which is in favor of guaranteeing a robust crystal structure and enhancing the cycling stability. On the other hand, there is no obvious oxidation/reduction peaks related to Mn^{3+}/Mn^{4+} pairs at around 2.5 V in CV plots for both cathodes, and previous studies have declared that Mn^{3+}/Mn^{4+} redox pairs participate in charge compensation below 2.5 V [6, 40, 47]. Hence, Mn^{3+}/Mn^{4+} pairs do not participate in the electrochemical reaction in NMNTM between 2.5 and 4.3V. The CV results are in good agreement with the charge/discharge profiles of NMNTM cathode in Fig. S3.

Fig. 4c-d exhibit ex situ XPS data and the fitting results of Ni-ion and Mn-ion after charging to 4.3 V and discharging to 2.5 V for the NMNTM cathode. The main peak located at ~ 854.6 eV can be ascribed to the Ni^{2+} ion in pristine powder NMNTM material, but it splits into two peaks that belong to Ni^{3+} and Ni^{4+} ions upon charging to 4.3 V[16, 23, 27, 32, 48], as shown in Fig. 4c. However, the main peak position does not move during the charge/discharge process in Fig. 4d, indicating that Mn^{4+} ions do not participate in the charge compensation upon extracting/inserting Na-ion[16, 32, 40, 48], consistent with CV results. Therefore, the Jahn-Teller distortion associated with high spin Mn^{3+} ions has been effectively suppressed though Mg and Ti co-doping, especially

Mg ions in the Na sites, which is beneficial for strengthening the lattice stability to enhance the cycling performance of NMNTM cathode, different from the NNM cathode [40]. Fig. S4 exhibits the XPS data of Na, Mg, O and Ti ions in pristine NMNTM powder material.

3.5 Structure evolution of NMNTM and Na-Ion Diffusion Coefficient Tests

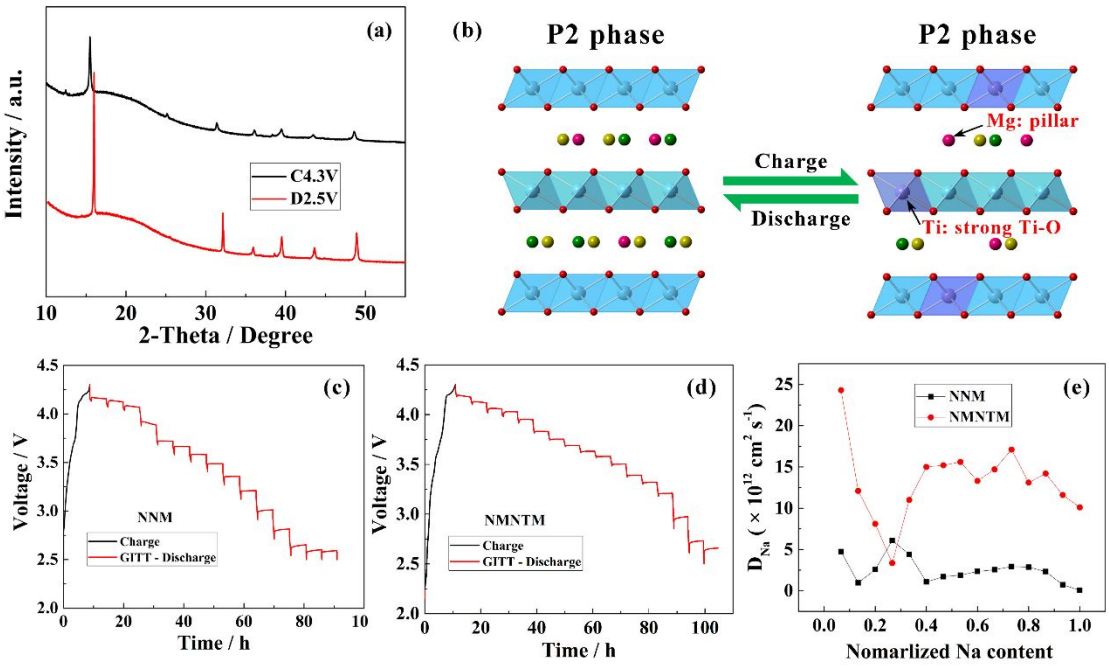

Fig. 5 (a) Ex situ XRD results of NMNTM cathode at different charged states and (b) structural evolution with phase-transition-free feature. GITT plots of (c) NNM and (d) NMNTM cathodes upon discharging at 0.1 C in the voltage range of 2.5 - 4.3 V, and (e) comparison of calculated Na-ion diffusion coefficients of both cathodes.

To unravel the structure evolution and analyze the step-like charge/discharge profiles of NMNTM cathode, ex situ XRD measurements were performed when being charged to 4.3 V and discharged to 2.5 V at 0.1 C. It can be found that NMNTM cathode maintains the P2 structure after charging to 4.3 V, Unlike the P2-O2 phase transition in NNM cathode[6, 40]. Ex situ XRD measurements confirm that there is no new phase beyond P2 structure, implying the phase-transition-free feature, as shown in Fig. 5a-b. Therefore, the step-like charge/discharge profiles in Fig. 3d are caused by superstructure ordering in NMNTM according to neutron diffraction and ex situ XRD

measurements. The enhanced cycling stability of NMNTM in Fig. 3f is also associated with the absence of phase transition upon charging and discharging.

To study the Na-ion diffusion kinetics after dual-site modulation of Mg/Ti ions, Galvanostatic Intermittent Titration Technique (GITT) were performed to calculate Na-ion diffusion coefficients, as shown in Fig. 4f-h. GITT tests were carried out during discharge process after a normal charge for 0.5 hours followed by a relaxation time of 5.0 hour and then a normal charge at 0.1 C. Therefore, Na-ion diffusion coefficients can be calculated according to the following equation[7, 32, 40, 49, 50]:

$$D_{Na} = \frac{4}{\pi\tau}\left(\frac{m_B V_M}{M_B S}\right)^2 \left(\frac{\Delta E_S}{\Delta E_\tau}\right)^2 \quad (1)$$

Where m_B, M_B and V_M correspond to the cathode mass, molecular weight and molar volume of NMNTM; S is the surface area here (0.785 cm^2), which is replaced with the geometrical area here. τ (s) is the testing time at each step. ΔE_s and ΔE_τ are the quasi-equilibrium potential and the change of voltage E during the current pulse, respectively. Fig. 5e compares the calculated Na-ion diffusion coefficients of both cathodes and Fig S5 shows the representative τ vs E profile for a single GITT titration analysis. The Na-ion diffusion is significantly promoted in NMNTM, with Na-ion diffusion coefficients primarily in the order of magnitude of 10^{-11} cm^2 s^{-1}. This is much higher than those of NNM cathode, which are typically in the order of magnitude of 10^{-12} cm^2 s^{-1}, as shown in Fig. 4h. Therefore, the improved rate capability of NMNTM is connected with the promoted Na-ion mobility after dual-site modulation of Mg/Ti ions.

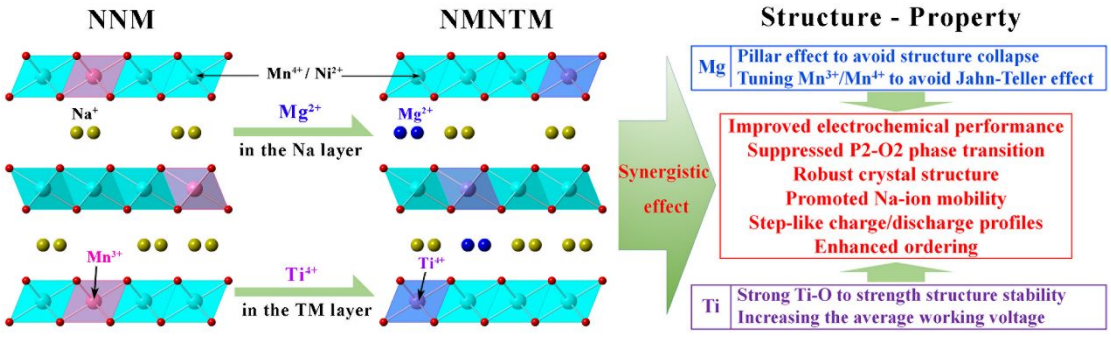

Fig. 6 Schematic illustration of synergistic effect of doped Mg and Ti ions in different crystallographic sites through dual-site modulation strategy

Fig. 6 further illustrates the dual-site modulation strategy to realize the synergistic effect of Mg/Ti-doping in Na and TM sites. To eliminate the Mn^{3+} ions in NNM (P2-$Na_{2/3}[Ni_{1/4}\ Mn^{3+}{}_{1/6}Mn^{4+}{}_{7/12}]O_2$) containing a mixture of Mn^{3+} and Mn^{4+} ions in structure, Mg^{2+} are incorporated into the Na-ion layer to ensure the charge neutrality by tuning the Mn^{3+}/Mn^{4+} ratio to eliminate Mn^{3+} ions, because Ti^{4+} ion share the same oxidation state with Mn^{4+} ions. Therefore, Mg and Ti ions in different crystallographic sites play various roles in achieving the synergistic effect during electrochemical cycling, thereby significantly improving the electrochemical performance of NMNTM cathode, as shown in Fig. 6.

4 Conclusions

In this study, Mg and Ti ions are employed to design a high-performance P2-$Na_{2/3}Mg_{1/18}[Ni_{1/4}Ti_{5/36}Mn_{11/18}]O_2$ (NMNTM) cathode material, through a dual-site modulation strategy of introducing Mg and Ti ions to the Na and transition-metal sites (Mn sites), respectively. Neutron diffraction reveals that NMNTM adopts a larger super cell structure model ($P6_3$ space group) due to the superlattice ordering in structure, and also identifies the different locations of Mg and Ti ions in Na and TM sites, respectively. Besides, enhanced ordering is also confirmed by neutron diffraction, which contributes the staircase-like charge/discharge profiles of NMNTM. In contrast, NMNTM delivers a reversible capacity of 113 mAh g^{-1}, corresponding to ~ 87% of its theoretical capacity and significantly improved rate capabilities of 96, 86, 61, 49 and 34 mAh g^{-1} at 1 C, 2 C, 5 C, 10 C and 15 C, respectively. Moreover, NMNTM displays an enhanced capacity retention of 80.2%, exceeding the 65.8% cycling stability of NNM after 150 cycles. CV and ex situ XPS tests demonstrate that only Ni^{2+}/Ni^{4+} redox couples participate in the electrochemical reaction while Mn^{4+} ions maintain the structural stability. Ex situ XRD measurements reveal that no new phase beyond P2 structure ais observed during the charge/discharge process, indicating the phase-transition-free feature of NMNTM cathode. The synergistic effect is stimulated by Mg and Ti ions in different crystallographic sites that significantly improves the electrochemical performance of

NMNTM, including the pillar effect of Mg-ion in the Na sites, phase-transition-free feature of NMNTM, suppressed Jahn-Teller effect by tuning the Mn^{3+}/Mn^{4+} ratio to eliminate Mn^{3+} ions, accelerated Na-ion movement by GITT tests, and enhanced crystal structure stability of strong chemical bond of Ti-O compared with Mn-O in the TM layers upon charging and discharging.

Conflicts of interest

The authors declare no competing financial interest.

Supplementary information

Supporting information includes the comparison of the neutron powder diffraction data of NNM and NMNTM sample using $P6_3/mmc$ and $P6_3$ space groups, SEM image of NNM sample, consistence between CV plots and charge/discharge profiles of NMNTM cathode at the second cycle at 0.1C within the voltage range of 2.5-4.3V, and refined crystal sites and atom occupancies of NNM and NMNTM samples based on XRD and NPD data, respectively.

Acknowledgements

This work was finically supported by the Foundation of China Institute of Atomic Energy (Grant No. YZ010270624220, Grant No. 16YZ202212000201), National Natural Science Foundation of China (Grant No. 12275362), Continuous-Support Basic Scientific Research Project (Grant No. BJ010261224864), and Ministry of Science and Technology of the People's Republic of China (Grant No. 2021YFA1600602).

References

1 W. Zuo and Y. Yang, *Acc. Chem. Res.*, 2022, **3**, 709-720.

2 J. Wang, Y.-F. Zhu, Y. Su, J.-X. Guo, S. Chen, H.-K. Liu, S.-X. Dou, S.-L. Chou and Y. Xiao, *Chem. Soc. Rev.*, 2024, **53**, 4230-4301.

3 W. Zuo, A. Innocenti, M. Zarrabeitia, D. Bresser, Y. Yang and S. Passerini, *Acc. Chem. Res.* , 2023, **56**, 284-296.

4 J. Zhang, W. Wang, W. Wang, S. Wang and B. Li, *ACS Appl. Mater. Interfaces*, 2019, **11**,

View Article Online
DOI: 10.1039/D5NR02365C

22051-22066.

5 Y.-J. Guo, R.-X. Jin, M. Fan, W.-P. Wang, S. Xin, L.-J. Wan and Y.-G. Guo, *Chem. Soc. Rev.*, 2024, **53**, 7828-7874.

6 L. F. Pfeiffer, Y. Li, M. Mundszinger, J. Geisler, C. Pfeifer, D. Mikhailova, A. Omar, V. Baran, J. Biskupek, U. Kaiser, P. Adelhelm, M. Wohlfahrt-Mehrens, S. Passerini and P. Axmann, *Chem. Mater.* , 2023, **35**, 8065-8080.

7 H. Fang, H. Ji, J. Zhai, C. Wang, C. Zhu, G. Chen, M. Chu, T. Zhang, Z. Ma, W. Zhao, W. Ji and Y. Xiao, *Small*, 2023, **19**, 2301360.

8 P.-F. Wang, T. Jin, J. Zhang, Q.-C. Wang, X. Ji, C. Cui, N. Piao, S. Liu, J. Xu, X.-Q. Yang and C. Wang, *Nano Energy*, 2020, **77**.

9 J. H. Stansby, W. M. Dose, N. Sharma, J. A. Kimpton, J. M. L. del Amo, E. Gonzalo and T. Rojo, *Electrochim. Acta*, 2020, **341**, 135978.

10 D. Wang, Y.-P. Deng, Y. Liu, Y. Jiang, B. Zhong, Z. Wu, X. Guo and Z. Chen, *Nano Energy*, 2023, **110**, 108340.

11 K. H. Wong, M. Zhang, T. Yang, Q. Ma, S. Dai, J. Wei, G. Kuma, A. A. AlHammadi, G. Karanikolos, E. Bekyarova, A. Elkamel and A. P. Yu, *Energy Storage Mater.*, 2024, **71**, 103549.

12 J. Billaud, G. Singh, A. R. Armstrong, E. Gonzalo, V. Roddatis, M. Armand, T. Rojo and P. G. Bruce, *Energy Environ. Sci.*, 2014, **7**, 1387-1391.

13 W. H. Zuo, J. M. Qiu, C. Y. Hong, X. S. Liu, J. L. Li, G. F. Ortiz, Q. Li, S. Y. Zheng, G. R. Zheng and Y. Yang, *ACS Appl. Energ. Mater.*, 2019, **2**, 4914-4924.

14 J. Liu, W. Huang, R. Liu, J. Lang, Y. Li, T. Liu, K. Amine and H. Li, *Adv. Funct. Mater.*, 2024, **34**, 2315437.

15 M. Yang, Z. Chen, Z. Huang, R. Wang, W. Ji, D. Zhou, T. Zeng, Y. Li, J. Wang, L. Wang, T. Yang and Y. Xiao, *Adv. Sci.*, 2024, **11**, 2404701.

16 W. Yin, Z. Huang, T. Zhang, T. Yang, H. Ji, Y. Zhou, S. Shi and Y. Zhang, *Energy Storage Mater.*, 2024, **69**, 103424.

17 X. Liu, W. Zuo, B. Zheng, Y. Xiang, K. Zhou, Z. Xiao, P. Shan, J. Shi, Q. Li, G. Zhong, R. Fu and Y. Yang, *Angew. Chem. Int. Ed.*, 2019, **58**, 18086-18095.

18 J.-J. Marie, M. Jenkins, J. Chen, G. Rees, V. Cellorio, J. Choi, S. Agrestini, M. Garcia-Fernandez, K.-J. Zhou, R. A. House and P. G. Bruce, *Adv. Energy Mater.*, 2024, DOI: https://doi.org/10.1002/aenm.202401935, 2401935.

19 L. T. Yang, L. Y. Kuo, J. M. L. del Amo, P. K. Nayak, K. A. Mazzio, S. Maletti, D. Mikhailova, L. Giebeler, P. Kaghazchi, T. Rojo and P. Adelhelm, *Adv. Funct. Mater.* , 2021, **31**, 2102939.

20 H. Yoshida, N. Yabuuchi, K. Kubota, I. Ikeuchi, A. Garsuch, M. Schulz-Dobrick and S. Komaba, *Chem. Commun.* , 2014, **50**, 3677-3680.

21 G. Singh, N. Tapia-Ruiz, J. Miguel Lopez del Amo, U. Maitra, J. W. Somerville, A. R. Armstrong, J. Martinez de Ilarduya, T. Rojo and P. G. Bruce, *Chem. Mater.* , 2016, **28**, 5087-5094.

22 J. W. Somerville, A. Sobkowiak, N. Tapia-Ruiz, J. Billaud, J. G. Lozano, R. A. House, L. C. Gallington, T. Ericsson, L. Haggstrom, M. R. Roberts, U. Maitra and P. G. Bruce, *Energy Environ. Sci.*, 2019, **12**, 2223-2232.

23 Z.-Y. Li, X. Ma, K. Sun, S. Ruan, G. Tian, W. Yang, J. Yang and D. Chen, *ACS Appl. Mater. Interfaces*, 2023, **15**, 17801-17813.

24 Z.-Y. Li, X. Ma, I. A. Bobrikov, K. Sun, H. Wang, L. He, Y. Li and D. Chen, *ACS Appl. Mater.*

View Article Online
DOI: 10.1039/D5NR02365C

Interfaces, 2022, **14**, 7869-7877.

25 Q.-C. Wang, J.-K. Meng, X.-Y. Yue, Q.-Q. Qiu, Y. Song, X.-J. Wu, Z.-W. Fu, Y.-Y. Xia, Z. Shadike, J. Wu, X.-Q. Yang and Y.-N. Zhou, *J. Am. Chem. Soc.*, 2019, **141**, 840-848.

26 J. Xu, D. H. Lee, R. J. Clement, X. Yu, M. Leskes, A. J. Pell, G. Pintacuda, X.-Q. Yang, C. P. Grey and Y. S. Meng, *Chem. Mater.*, 2014, **26**, 1260-1269.

27 Y. Wen, Z. Huang, J. Le, P. Dai, C. Shi, G. Li, S. Zhou, J. Fan, S. Zhuang, M. Lu, L. Huang and S.-G. Sun, *ACS Appl. Mater. Interfaces*, 2022, **14**, 29813-29821.

28 J. Huang, J. Gao, N. Hong, B. Zhang, H. Wang, F. Zhu, L. Ni, G. Zou, H. Hou, H. Chen, W. Deng and X. Ji, *Nano Energy*, 2024, **126**, 109676.

29 Y. Wang, R. Xiao, Y.-S. Hu, M. Avdeev and L. Chen, *Nat. Commun.*, 2015, **6**, 6954.

30 P.-F. Wang, H.-R. Yao, X.-Y. Liu, Y.-X. Yin, J.-N. Zhang, Y. Wen, X. Yu, L. Gu and Y.-G. Guo, *Sci. Adv.* , 2018, **4**, eaar6018.

31 N. Ortiz-Vitoriano, N. E. Drewett, E. Gonzalo, B. Acebedo, F. J. Bonilla, J. M. Lopez del Amo, J. H. Stansby, N. Sharma, O. Lakuntza, J. Carrasco and T. Rojo, *J. Mater. Chem. A* 2019, **7**, 21812-21826.

32 J. Jin, Y. Liu, Q. Shen, X. Zhao, J. Zhang, Y. Song, T. Li, X. Xing and J. Chen, *Adv. Funct. Mater.*, 2022, **32**, 2203424.

33 T. Zhang, H. Ji, X. Hou, W. Ji, H. Fang, Z. Huang, G. Chen, T. Yang, M. Chu, S. Xu, Z. Chen, C. Wang, W. Yang, J. Yang, X. Ma, K. Sun, D. Chen, M. Tao, Y. Yang, J. Zheng, F. Pan and Y. Xiao, *Nano Energy*, 2022, **100**, 107482.

34 L. Geng, L. Wu, H. Tan, M. Wang, Z. Liu, L. Mou, Y. Shang, D. Yan and S. Peng, *Nanoscale*, 2024, **16**, 9488-9495.

35 C. L. Zhao, Z. P. Yao, Q. D. Wang, H. F. Li, J. L. Wang, M. Liu, S. Ganapathy, Y. X. Lu, J. Cabana, B. H. Li, X. D. Bai, A. Aspuru-Guzik, M. Wagemaker, L. Q. Chen and Y. S. Hu, *J. Am. Chem. Soc.*, 2020, **142**, 5742-5750.

36 T. Jin, P. F. Wang, Q. C. Wang, K. J. Zhu, T. Deng, J. X. Zhang, W. Zhang, X. Q. Yang, L. F. Jiao and C. S. Wang, *Angew. Chem. Int. Ed.*, 2020, **59**, 14511-14516.

37 Z.-Y. Li, H. Wang, W. Yang, J. Yang, L. Zheng, D. Chen, K. Sun, S. Han and X. Liu, *ACS Appl. Mater. Interfaces*, 2018, **10**, 1707-1718.

38 H. R. Yao, P. F. Wang, Y. Gong, J. N. Zhang, X. Q. Yu, L. Gu, C. Y. OuYang, Y. X. Yin, E. Y. Hu, X. Q. Yang, E. Stavitski, Y. G. Guo and L. J. Wan, *J. Am. Chem. Soc.*, 2017, **139**, 8440-8443.

39 Z.-Y. Li, X. Ma, K. Sun, L. He, Y. Li and D. Chen, *ACS Appl. Energy. Mater.*, 2022, **5**, 1126-1135.

40 Z.-Y. Li, X. Ma, K. Sun, F. Ning, L. Sun, G. Tian, J. Gao, H. Wang and D. Chen, *J. Mater. Chem. A*, 2024, **12**, 26113-26124.

41 N. Ahmad, L. Yu, M. U. Muzaffar, B. Peng, Z. Tao, S. Khan, A. Rahman, J. Liang, Z. Jiang, X. Ma and G. Zhang, *Adv. Energy Mater.*, 2025, **15**, 2404093.

42 Y. Wang, Z. Feng, P. Cui, W. Zhu, Y. Gong, M.-A. Girard, G. Lajoie, J. Trottier, Q. Zhang, L. Gu, Y. Wang, W. Zuo, Y. Yang, J. B. Goodenough and K. Zaghib, *Nat. Commun.* , 2021, **12**, 13.

43 K. Kubota, T. Asari and S. Komaba, *Adv. Mater.*, 2023, **35**, 2300714.

44 Z.-Y. Li, F. Ning, X. Ma, K. Sun, L. Sun, H. Wang and D. Chen, *Energy Storage Mater.*, 2025, **76**, 104114.

45 R. A. House, U. Maitra, M. A. Pérez-Osorio, J. G. Lozano, L. Jin, J. W. Somerville, L. C. Duda, A. Nag, A. Walters, K. J. Zhou, M. R. Roberts and P. G. Bruce, *Nature*, 2020, **577**, 502-508.

46 C. Zhao, Y. Lu, L. Chen and Y.-S. Hu, *Nano Res.*, 2019, **12**, 2018-2030.

47 R. Luo, F. Wu, M. H. Xie, Y. Ying, J. Zhou, Y. Huang, Y. Ye, L. Li and R. Chen, *J. Power Sources*, 2018, **383**, 80-86.

48 B. Peng, Y. Chen, F. Wang, Z. Sun, L. Zhao, X. Zhang, W. Wang and G. Zhang, *Adv. Mater.*, 2022, **34**, 2103210.

49 P. Zou, L. Yao, C. Wang, S. J. Lee, T. Li and H. L. Xin, *Angew. Chem. Int. Ed.*, 2023, **62**, e202304628.

50 C. Zhao, F. Ding, Y. Lu, L. Chen and Y.-S. Hu, *Angew. Chem. Int. Ed.*, 2020, **59**, 264-269.

View Article Online
DOI: 10.1039/D5NR02365C

Data availability statement

The authors confirm that all relevant data are available within the article and the ESI. And the pristine data in this current study are available from the corresponding author on reasonable request.